

Inclusion Behavior During the Electron Beam Button Melting Test

J.P. Bellot, B. Defay, J. Jourdan, P. Chapelle, and A. Jardy

(Submitted July 14, 2011)

The high mechanical performance of alloys developed for the manufacture of turbine disks depend upon the size and the number density of the inclusions. The electron beam button method has been practiced since the 1980s as a technique to quantify the cleanliness of the superalloys as well as to identify the nature and the size of the inclusions. The technique involves melting the sample into a hemispherical water-cooled crucible and the low density inclusions (mainly oxides) are concentrated by a combination of Marangoni and buoyancy forces into an area at the top surface of the button referred to as the raft. We have experimentally studied the behavior of oxide inclusions in special steels using both high definition video and infrared cameras. We have observed the inversion of the Marangoni effect due to the presence of sulfur, which leads to a positive temperature coefficient of the surface tension. A mathematical modeling has been carried out to simulate the turbulent fluid flow associated with the temperature field in the metallic pool of the button. The surface temperature profile has been successfully compared with the measured data. A post-processor numerical tool calculates the inclusion trajectories taking into account the turbulent fluctuation velocity by a stochastic approach. Hence, the behavior of a population of inclusions has been statistically studied, and the dependence of the capture efficiency on the inclusion size has been analyzed.

Keywords advanced characterization, aerospace, superalloys

1. Introduction

Since the end of the last century, the reduction of the weight of high performance materials together with the improvement of mechanical properties and the increase of the recycling of used metals have been new challenges which emphasize the importance of metal cleanliness. For various metallic materials [steel (Ref 1), aluminum (Ref 2, 3), titanium (Ref 4)...], noticeable research efforts in France have been made over the last decade with the aim of improving the efficiency of the liquid metal treatments to remove inclusions. The metal cleanliness is, however, difficult to quantify because it is defined as a distribution function of internal variables, such as the size, the composition, or even the porosity or the fractal dimension. Moreover, the very low volume fraction of inclusions in superclean materials (e.g., some special steels, nickel-based superalloys where the fraction can be lower than 1 ppm) and the small size of the inclusions (few μm) make the use of non-destructive methods for cleanliness evaluation such as the ultrasonic inspection inefficient.

For conventional steels, the universal assessment technique for inclusions remains quantitative metallography, following different standards: ASTM, DIN, or JST rating method. The

technique is based on either manual or automated visualization of representative area of the samples, and Hénault (Ref 5) has developed a statistical analysis of extreme values. The main drawback of the method appears to lie in the small volume examined. Indeed, as the number of inclusions in the material decreases, a larger volume of alloy must be examined to obtain results which have statistical significance and the analysis of large surfaces becomes rapidly time consuming. Large size inclusions are even more concerned by this drawback because the largest inclusions have the lowest frequency in the PSD (particle size distribution). Hence, in typical Maraging steel, the PSD indicates that the identification of the largest inclusions would require a sample volume of the order of 1 kg corresponding to the unrealistically large 2D examination area.

In this unsatisfactory situation, the electron beam button-melting (EBBM) is a potential alternative. This method had been initially used in the 1970s as a cleanliness assessment method for nickel-based superalloys and a tool to assist in the development of various melting techniques (VIM, ESR, and VAR) which were studied by Sutton and Clark (Ref 6) and Sutton and Mancuso (Ref 7). Among the studies published in the literature, a large part deals with the effect of surface-active elements (especially O or S) on the efficiency of the test to collect inclusions. Quested et al. (Ref 8) concluded that a proper raft formation is associated with melts having sulfur contents greater than 10 ppm. In the same way, Halali et al. (Ref 9) demonstrated that the addition of flux (oxides) leading to the reduction of sulfur content can reverse the Marangoni convection and modify the inclusion collection. In the present article, we will show and argue that new EBBM technology could lead to a contrasting conclusion. In addition, several studies have been performed to make the EBBM technique a standard method such as ASTM standard. Unfortunately, these attempts failed mainly because of the lack of the reproducibility

J.P. Bellot, J. Jourdan, P. Chapelle, and A. Jardy, Institut Jean Lamour (UMR 7198), Ecole des Mines de Nancy, 54042 Nancy Cedex, France; and B. Defay, Snecma Gennevilliers, Service YQGC, 171 quai Valmy—BP31, 92700 Colombes Cedex, France. Contact e-mail: Jean-Pierre.Bellot@mines.inpl-nancy.fr.

of the test. Finally, Mitchell et al. (Ref 10) put forward that this technique does not produce a complete spectrum of inclusion sizes, but only measures the amount of inclusions with a size greater than 4-5 μm . Since the larger inclusions represent a small fraction of the oxygen content in steels, Mitchell explains that it is unrealistic to directly relate the alloy oxygen content to the inclusion content measured by EBBM.

In the next section, the EBBM technique is described in detail. In particular, the flexibility of the guidance of the electron beam in modern electron guns is highlighted since this feature contributes to the improvement of the test. The important role of the Marangoni flow is demonstrated by the comparison of two tests distinguished by the sulfur content. Finally, the use of numerical modeling casts new light on the thermo-hydrodynamic behavior of the bath and on the inclusion trajectories. The efficiency of the technique as a function of the inclusion size in particular is determined.

2. Description of the EBBM Test

The EBBM technique uses an electron beam as the heat source with the aim of melting the sample (approximately 1 kg) and collecting the low density inclusions into a raft at the surface of the pool. The EBBM unit used was an ALD EBLab100 which is schematically presented in Fig. 1. It includes a vacuum chamber (with a pressure lower than 10^{-3} mbar) and an EB gun with an accelerating voltage of 40 kV. The chamber is equipped with a hemispherical water-cooled copper crucible (see Fig. 1) to hold the sample.

At the beam impingement point (10 mm in diameter), the kinetic energy of the electrons is converted into thermal energy (between 50 and 70% depending of the alloy), and the backscattering of electrons results in important losses as demonstrated by Shiller (Ref 11). Goldak et al. (Ref 12) and later Wei and Chow (Ref 13) have shown that, at any instant, the electron beam deposits the heat with a Gaussian distribution centered at the beam impingement point. The total electrical power applied is usually in the range between 10 and 20 kW.

In order to distribute the heat power, the beam executes a motion (with a very high frequency up to 2 kHz) in the form of one or more circles on the surface of the sample owing to the use of magnetic lenses. This beam guidance is very important because it allows to heat either the center of the sample (as it was performed in the past with a fixed beam [Quested et al. (Ref 8)]) or to heat the sample periphery (with a large circle).

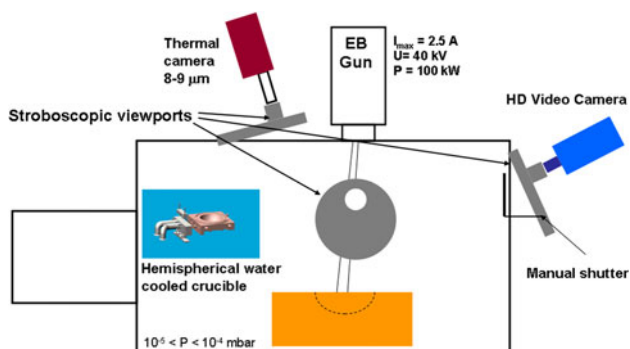


Fig. 1 Schematic diagram of the electron beam furnace

In order to analyze the thermal evolution of the sample and the inclusion behavior during the test, several optical techniques have been employed through a port with a stroboscopic window to reduce the accumulation of condensed metal vapor. The acquisition of the temperature of the pool surface was done using both a 2-wavelength pyrometer (IRCON[®] Modline Type-R) and an infrared thermo camera (ThermaCAM SC300—FLIR). The quantum detector of the thermo camera, which is in gallium arsenide, operates in an infrared strip between 8 and 9 μm , and enables carrying out temperature measurements up to 2000 °C. The pictures of the inclusion raft are recorded by a high definition video camera (Sony FX1000E), and the image processing is realized using Photoshop and Aphelion softwares. After button cooling, the optical and scanning electron microscopes are used for the characterization of the inclusion raft.

The melting cycle used in the present EBBM tests consisted of the following steps:

1. The electron beam power is regularly increased to melt the sample and to obtain a liquid pool as large as possible. During this first step, several scanning patterns (circles) of the beam over the free surface of the pool can be applied to optimize the melting depending on the initial shape of the sample.
2. In the second step, the maximal beam power is sustained, and the raft formation is controlled by the direction of the thermocapillary flow.
3. The melting test is terminated after 5 min by progressively reducing the power until complete solidification of the sample, following which the power is turned off. After cooling, the sample with a spherical cap shape (called “button”) is directly transferred to optical or SEM analysis without any cleaning or preparation.

3. Experimental Results

3.1 Example of a Superalloy

A series of tests were carried out on a nickel-based superalloy. The maximal power during the temperature stable period was 17 kW, this value being on the higher side for the electron beam button melting test. During this period, the electron beam scanned a large circle of 8 cm in diameter. The mass of the metal sample was 760 g. The field of the surface temperature of the metal bath obtained by infrared thermography during the temperature stable period, as well as a temperature profile along the diameter of the bath, are shown on Fig. 2. The metal emissivity (assumed to be constant) was determined in a separate calibration experiment, which consisted in measuring the evolution of the temperature of a liquid metal sample during its cooling (in particular its solidification) and comparing the temperature data collected by infrared thermography and by a bichromatic pyrometer. The calibrated value of the emissivity was 0.19.

In Fig. 2, the thin crown of metal, remaining solid at the button periphery, appears with a violet-blue color. The thermal imprint of the electron beam can be seen as a circular surface of 8-cm diameter. The raft of inclusions is also clearly apparent (with a white color), because of the likely much greater emissivity of the inclusions compared to that of the liquid

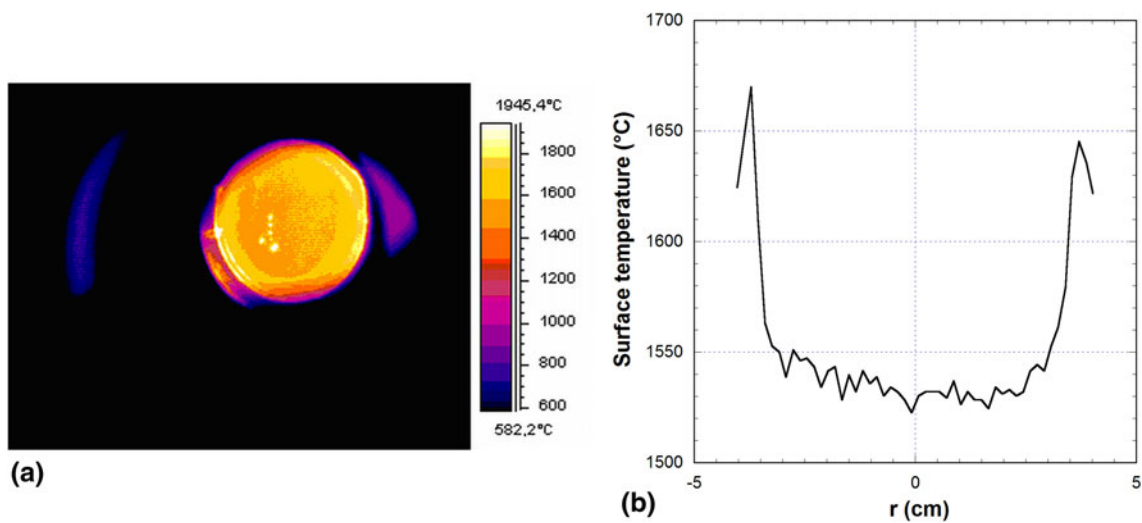


Fig. 2 Field of the surface temperature of the metal bath (left) and temperature profile along a diameter of the bath (right) during the temperature stable period

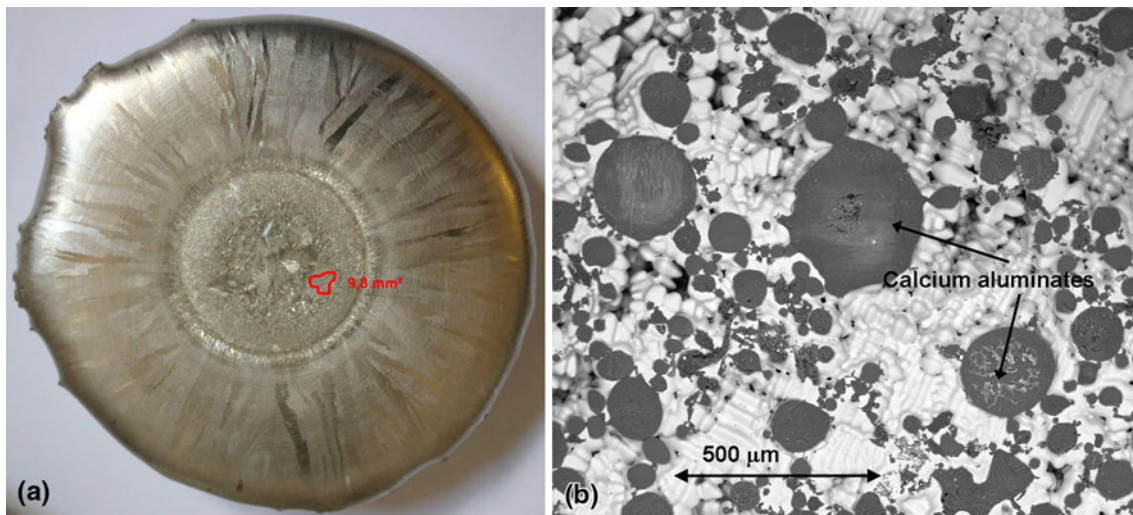


Fig. 3 Left: Photograph of the top surface of a solidified button of nickel-based superalloy. The area of the inclusion raft is marked with a red line. Right: Image of the raft of calcium aluminates observed by SEM (Color figure online)

metal. It should be mentioned that the measurements in the size of the raft from the images recorded by a video camera, which provides a much higher spatial resolution, were found to be much more accurate than those from the images recorded by the thermo camera. Finally, it is noticed that the surface temperature is relatively uniform and that the superheat temperature (with respect to the liquidus temperature of the alloy: $T_{liq} = 1365^{\circ}\text{C}$) reaches nearly 300°C under the impact of the electron beam.

A photograph of a typical solidified button is given in Fig. 3. The raft of inclusions is located near the center of the button and its area remains small.

A chemical analysis using energy dispersive x-ray spectrometry and an electron probe microanalyzer has revealed that the inclusions are calcium aluminates. Owing to the high values of the temperature reached during the test, these inclusions were partially liquid during their collection and gathering at the bath surface. In the solidified button, they are plate shaped, with

a characteristic dimension of relative importance (superior to $10\ \mu\text{m}$).

Figure 4 presents a macrography of a vertical section of a solidified button, where the profile of the liquid pool during the test has been located from the microstructure and is marked with a yellow line. This figure shows that the volume of the metal bath was very close to the volume of the metal sample. This point is important to insure that almost all the inclusions present in the metal sample can potentially be collected during the test.

3.2 Example of Two Steel Alloys

In this paragraph, we compare the behavior of two special steel alloys, which differ in their sulfur contents. During the two tests, the electron beam power was 13.6 kW, and the scanning pattern of the electron beam consisted of two circles of diameters 2.6 and 8 cm.

The video images in Fig. 5 illustrate the important influence of surfactants like sulfur. On the left image (low sulfur content), the oxide particles are kept by the Marangoni surface flows in the region within the two circles scanned by the electron beam. In contrast, in the 27CrMo4 steel bath presented on the right image, sulfur content of which is much higher (larger than 0.02 wt.%), the oxide particles are entrained under the beam impacts where they tend to gather.

4. Thermo-Hydrodynamic Behavior of the Liquid Pool

4.1 Marangoni Convection

The motion of the liquid metal combines two phenomena: the thermal natural convection and the thermocapillary convection called Marangoni convection as will be described briefly.

Local surface temperature gradients in the bath can lead to surface tension gradients. These gradients give rise to shear stresses. The latter produce surface flows from regions of low-to-high surface tensions that initiate circulation flows within the molten pool.

$$\tau_{zr} = \left(\frac{\partial \gamma}{\partial T} \right) \left(\frac{\partial T}{\partial r} \right) = \mu_{\text{eff}} \frac{\partial u_r}{\partial z} \quad (\text{Eq 1})$$

The direction and magnitude of the thermocapillary flow are determined by the concentration of surface-active elements (especially elements of the group VI such as O and S) present in the alloy. These elements have two effects:

- The surface active elements cause a dramatic reduction in surface tension γ ,
- The temperature dependence $\frac{\partial \gamma}{\partial T}$ changes from a negative value (the liquid metal flows from hotter toward cooler regions) to a positive value (which results in a reverse motion of the liquid metal). The temperature dependence of surface tension for stainless steel alloys is given by Li et al. (Ref 14).

In the EBBM test, the thermal power at the beam impingement point produces high temperature gradients which can reach values close to 10^4 °C/m. Moreover, the temperature gradients are enhanced by the cooling of the metal in contact with the cold crucible wall.

The relative importance of thermal natural and thermocapillary convections can be characterized by calculating the ratio of the Rayleigh number to the Marangoni number:

$$G = \frac{Ra}{Ma} \quad A = \frac{\rho g \beta_T h^2}{\gamma_T} \quad (\text{Eq 2})$$

where A is the aspect ratio of the pool, and β_T is the thermal expansion coefficient. The group G has been discussed in many contexts by Yang (Ref 15) and by Gillon and Homay (Ref 16). It has the advantage of being independent of the applied temperature difference. For EBBM application, G is around 10, which means that the natural convection should play the major role. However, this conclusion must be qualified since the application of the heat source on the top of the pool stabilizes the flow and contributes to thermal stratification. Indeed, we will see that with the numerical simulations, if natural convection is effectively responsible for the bulk flow, then the surface flow mainly results from Marangoni effect.

4.2 Numerical Simulation

The thermo-hydrodynamic behavior of the liquid pool is simulated using an in-house finite volume code developed in our Institute [Bellot et al. (Ref 17)]. The main features of the mathematical model are reproduced here.

The code solves the coupled transport equations of heat and momentum in a 2D axisymmetrical geometry. The incompressible Navier-Stokes equations are expressed in terms of the



Fig. 4 Macrograph of a sectioned button of nickel-based superalloy

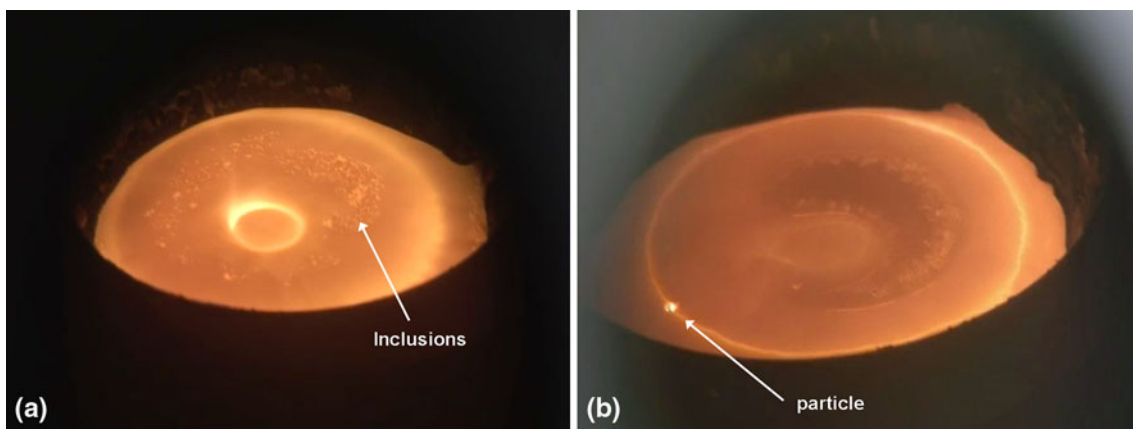


Fig. 5 Video images of the metal bath surface during the electron beam button melting test of a Maraging steel (left) and a 27CrMo4 steel (high sulfur content) (right)

stream function and the vorticity, and a $k-\epsilon$ turbulence model is implemented. The thermal natural and the thermocapillary convections, which are the only two sources of the flow, are modelled. A precise description of the power distribution beneath the beam and its movement over the bath surface are incorporated in the model. At its point of impact with the bath, the beam energy is assumed to have a Gaussian distribution [Wei and Chow (Ref 13)], while the beam describes a circular scanning pattern. The liquid pool surface is assumed to be flat.

In the first step, we have simulated the thermo-hydrodynamic behavior of the superalloy in the EBBM test carried out in our laboratory furnace (see Fig. 2).

The turbulent fluid flow provides a relatively uniform pool temperature with a hot spot at the beam location near the edge of the button. Marangoni and thermal natural convections drive the motion of the liquid pool with a maximal velocity of around 10 cm/s which is reached at the periphery of the pool where temperature gradients are the highest. The right-hand side of the Fig. 6 emphasizes that the profiles of the calculated and measured surface temperatures match well, which validates the model.

In order to assess the capture efficiency of inclusions depending on the sulfur content of the metal, the thermo-hydrodynamic behavior of the pool was simulated in two cases, with (Maraging steel and 27CrMo4 steel) all the operating conditions remaining identical.

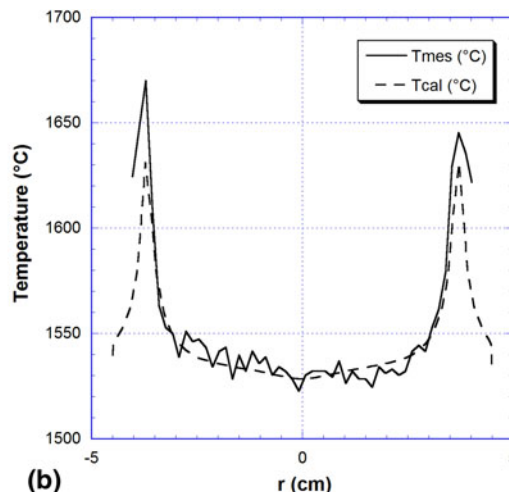
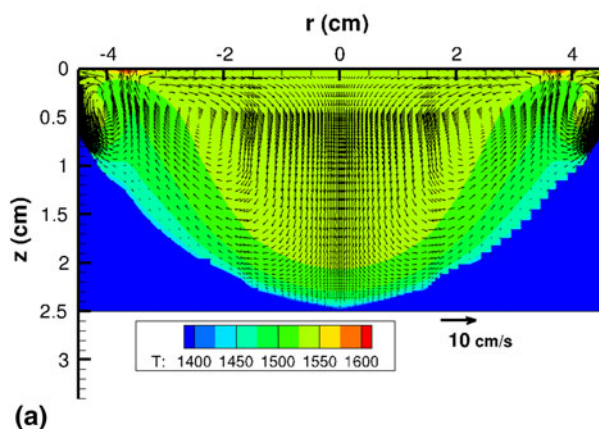


Fig. 6 Numerical simulation of the pool behavior in EBBM test of a superalloy. Left: Contour map of temperature (°C) and velocity vectors (cm/s)—right: surface temperature (°C) measured and calculated

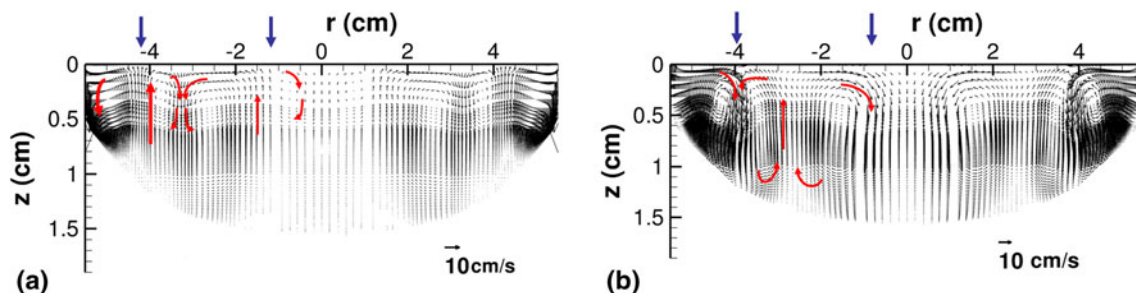


Fig. 7 Comparison of velocity fields (the dimensions are in cm, and the velocities are in cm/s). On the left: Maraging steel ($d\gamma/dT = -0.29$ mN/m/K), and on the right: 27CrMo4 steel ($d\gamma/dT = 1.4$ mN/m/K)

Figure 7 clearly shows an opposite structure of the flow in the two cases. In the half section of the button, we notice four alternated rotating flows when $d\gamma/dT < 0$ (left hand side, Maraging steel without sulfur content), while three alternated rotating flows are observed when $d\gamma/dT > 0$ (right hand side, 27CrMo4 steel with a sulfur content larger than 0.02 wt.%). The liquid alloy flows from the hotter regions (at the beam impingement point marked by the blue arrows in Fig. 7) toward cooler regions in the first case, and inversely in the presence of a surface active element.

Another illustration of the Marangoni effect is highlighted in Fig. 8 with the comparison of the radial surface flow in the two cases. We notice that the radial velocity is close to zero at the impact of the beam ($r = 4$ cm), but with a positive derivative in the case without sulfur content (solid line) and a negative derivative in the experiment with a high sulfur content (dotted line). These simulations readily explain the inclusion behavior experimentally observed on Fig. 5 where the oxide particles have an erratic motion between the two circles scanned by the electron beam (for the Maraging steel) whereas the oxide particles traveled across the pool to accumulate and agglomerate under the beam in the case of high sulfur content.

Therefore and unlike the Quested' conclusions (Ref 8), an alloy with a total S content below the critical concentration (i.e., few ppm) has the advantage of not sintering the inclusions under the beam but of moving them away toward the cooler

regions. The best practice of the EBBM test consists in applying a large circle as the beam pattern and collecting the inclusions in a central raft, taking advantage of the thermocapillary radially inward flow.

5. Inclusion Behavior

5.1 Modelling

The trajectories of inclusions are calculated by solving the fundamental dynamics equation taking into account the buoyancy forces (weight and Archimede), the drag and the added mass forces. The drag coefficient is expressed by the Morsi and Alexander correlation (Ref 18). In order to model the turbulent dispersion of the particles, we have used the ARMA method (AutoRegression Moving Average), which considers the fluctuation velocity of the liquid nearby the particle taking into account the Eulerian temporal correlation calculated from the local values of k and ϵ . Details of this efficient process will be found in the Petrisan' thesis (Ref 19) and more recently in the Quatravaux' thesis work (Ref 20). The fluid flow is not affected

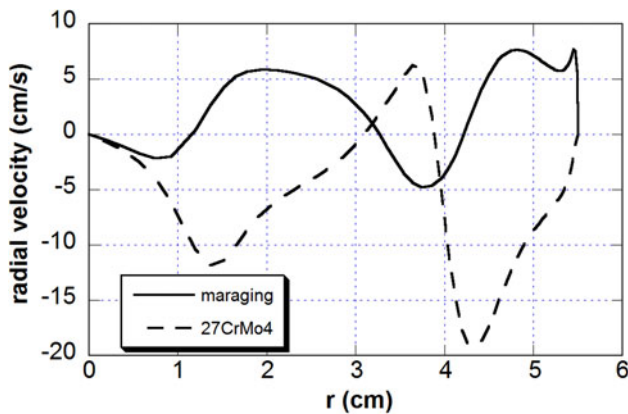


Fig. 8 Comparison of the radial velocity profiles for a Maraging steel (solid line) and a 27CrMo4 steel (dotted line)

by the motion of the inclusions owing to their small weight fraction, and the trajectories are accordingly simulated after completion of the liquid metal flow calculation. Moreover, the small volume fraction of inclusions allows us to neglect the interaction between particles. An inclusion is assumed to be captured (either by the solidification front or by the liquid surface) if the distance between the particle and the interface is smaller than the particle radius. The fundamental dynamics equation is integrated by an explicit Runge-Kutta algorithm.

5.2 Simulations and Statistical Results

In the example of the superalloy EBBM, trajectories were calculated for a wide range of particle sizes. Figure 9 presents two trajectories among them which emphasize the importance of the buoyancy forces for inclusion size of 100 μm whereas a more chaotic motion and flow dependant, (see the hydrodynamics of the pool in Fig. 6) is obtained for a 2- μm size inclusion.

From the findings of Fig. 9, we could believe that a small particle will more likely be entrapped by the solidification front rather than a larger one. In order to judge whether this statement is true or not, a set of 1000 trajectory runs has been achieved for each particle size. Figure 10 indicates the influence of the inclusion size on the respective probabilities of entrapment of the particles at the pool surface and at the solidification front. Although the inclusions smaller than 10 μm may have 5-10% chance to be captured by the solidification front, the EBBM test appears to be a viable method to gather most of the inclusion population into a raft at the free surface of the pool and finally to produce a complete spectrum of inclusion sizes. Moreover, the dwell time distribution of the oxide inclusions indicates that, whatever the particle size, the maximum dwell time reaches 30-40 s; so the duration of the test (4-5 min) guarantees the capture of all the inclusions.

6. Conclusion

Nowadays, the EB button melting remains the main test used to measure the amount of large inclusions present in

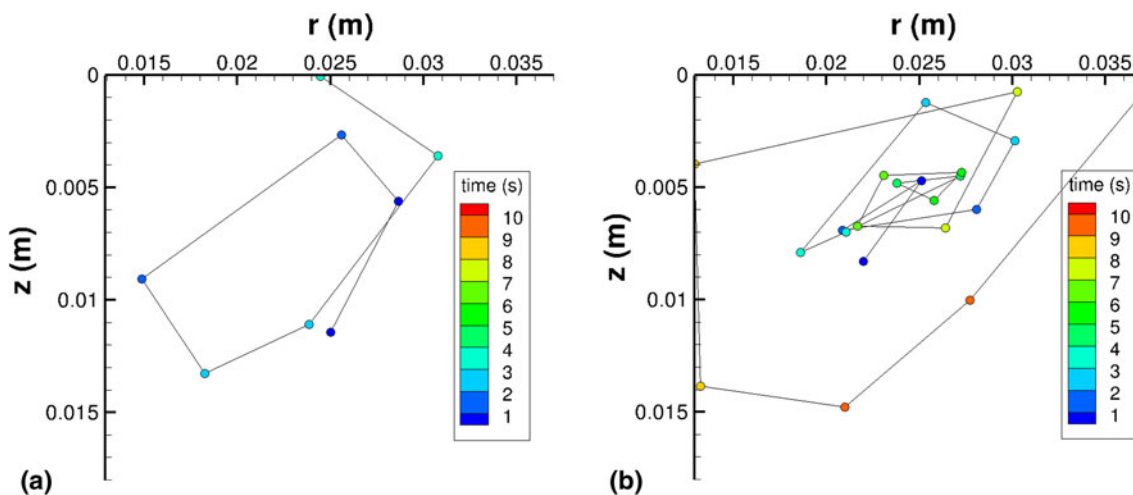


Fig. 9 Example of inclusion trajectories, each marker locates the particle at time interval equal to 0.5 s. Inclusion size of 100 μm (left) and 2 μm (right)

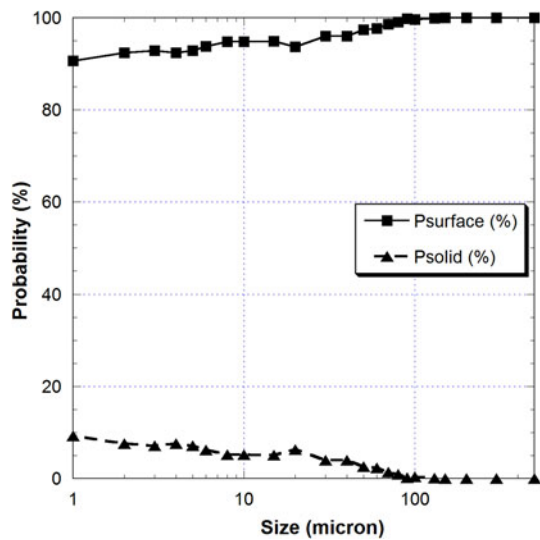


Fig. 10 Probability of capture (%) of the inclusions at the pool surface or at the solidification front as a function of size

significant size superalloy samples. We have demonstrated thanks to experimental observations confirmed by numerical simulation of the thermo-hydrodynamic of the pool that the Marangoni flow plays a major role in the raft formation although thermal natural convection governs the bulk flow. When the S content is higher than a critical value, the capillary flow causes the inclusions to move under the beam where they experience high temperatures, leading to possible sintering of the particles. This may have evident disadvantage with regard to the determination of the particle size distribution. On the contrary, when the S content lies below this critical level, the large circle scanned by the electron beam concentrates the inclusions into a raft at the centre of the free surface, where the low superheat temperature reduces the partial melting or decomposition of the inclusions. The behavior of the inclusions within the liquid pool has been investigated by intensive calculation of trajectories. The simulations clearly show a size dependence of the particle motion. Inclusions larger than 100 μm move mainly under the influence of buoyancy forces whereas inclusions of a few μm or less mainly follow the turbulent liquid flow. Despite this difference, most of the inclusion trajectories cross the free surface of the pool, so that the majority of the inclusions are potentially collected into a raft. Only 10% of the inclusions smaller than a few μm touch the solidification front. Further investigation on the efficiency of the capture of the inclusions at the interfaces could validate this conclusion.

References

1. I.L.A. Daoud, N. Rimbart, A. Jardy, B. Oesterlé, S. Hans, and J.P. Bellot, 3D Modelling of the Aggregation of Oxide Inclusions in a Liquid Steel Ladle: Two Numerical Approaches, *Adv. Eng. Mater.*, 2011, **13**, p 543–549
2. O. Mirgaux, D. Ablitzer, E. Waz, and J.P. Bellot, Mathematical Modelling and Computer Simulation of Molten Aluminium Purification by Flotation in Stirred Reactor, *Metal. Mater. Trans. B*, 2009, **40B**, p 363–375
3. H. Duval, C. Rivière, E. Lae, P. Le Brun, and J.B. Guillet, Pilot-Scale Investigation of Liquid Aluminum Filtration Through Ceramic Foam Filters, *Met. Trans. B*, 2009, **40(2)**, p 233–246
4. J.P. Bellot, B. Foster, S. Hans, E. Hess, D. Ablitzer, and A. Mitchell, Aluminium Volatilization and Inclusion Removal in the Electron Beam Cold Hearth Melting of Ti Alloys, *Metall. Mater. Trans. B*, 2000, **31B**, p 845–854
5. E. Hénault, A Statistical Method to Assess the Reliability of Cleanliness Measurements for High Quality Bearing Steels, *J. ASTM*, 2006, **3**, p 10–15
6. W.H. Sutton and I.D. Clark, Development of an EB Melting Test to Evaluate the Cleanliness of Superalloys, *Proceedings of the Conference on Electron Beam Melting and Refining – State of the Art 1983* (Reno, NV, USA), Bakish Corp., Englewood, 1983, p 36–61
7. W.H. Sutton and S.O. Mancuso, Evaluation of Filter Performance in Purifying MM-200 Plus HfMETALS by the EB-Button Test, *Proceedings of the Conference on Electron Beam Melting and Refining – State of the Art 1983* (Reno, NV, USA), Bakish Corp., Englewood, 1985, p 330–355
8. P.N. Qusted, D.M. Hayes, and K.C. Mills, Factors Affecting Raft Formation in Electron Beam Buttons, *Mater. Sci. Eng.*, 1993, **A173**, p 371–377
9. M. Halali, M. McLean, and D.R.F. West, Effect of Flux Additions on Inclusion Removal and Microstructure in Electron Beam Button Melting of Udimet 720, *Mater. Sci. Technol.*, 2000, **16(4)**, p 457–462
10. A. Mitchell, E. Samuelsson, and G. Silda, Assessment of Oxide Inclusions in Steels by EB Button Melting, *Proceedings of the Conference on Electron Beam Melting and Refining – State of the Art 1983* (Reno, NV, USA), Bakish Corp., Englewood, 1985
11. S. Shiller, U. Heisig, and S. Panzer, *Electron Beam Technology*, Wiley, New York, 1982
12. J. Goldak, A. Chakravarti, and M. Bibby, A New Finite Element Model for Welding Heat Sources, *Met. Trans. B*, 1984, **15**, p 299–305
13. P.S. Wei and Y.T. Chow, Beam Focussing Characteristics and Alloying Element Effects on High-Intensity Electron Beam Welding, *Met. Trans. B*, 1992, **23**, p 81–90
14. Z. Li, K. Mukai, and M. Zele, Determination of the Surface Tension of Liquid Stainless Steel, *J. Mater. Sci.*, 2005, **40**, p 2191–2195
15. H.Q. Yang, Boundary Effect on the Benard-Marangoni Instability, *J. Heat Mass Transf.*, 1992, **35**, p 2413–2420
16. P. Gillon and G.M. Homay, Combined Thermocapillary-Buoyancy Convection in a Cavity: An Experimental Study, *Phys. Fluid*, 1996, **8(11)**, p 2953–2963
17. J.P. Bellot, A. Jardy, and D. Ablitzer, Simulation numérique des transports couplés au sein du puits liquide d'un lingot de titane refondu par bombardement électronique, *Revue de Métallurgie - C.I.T./Science et Génie des Matériaux*, 1995, **92(12)**, p 1399–1410
18. S.A. Morsi and A.J. Alexander, An Investigation of Particle Trajectories in Two-Phase Flow Systems, *J. Fluid Mech.*, 1972, **55**, p 193–208
19. A. Petrisan, Sur les modèles stochastiques lagrangiens de suivi de particules dans un champ turbulent, Thèse Université Henri Poincaré, Nancy, France, 2001
20. T. Quatravaux, Evolution de la modélisation du procédé VAR, Thèse Institut National Polytechnique de Lorraine, Nancy, France, 2004